

X-ray in-line phase microtomography for biomedical applications

M. Langer^{1,2,3}, R. Boistel^{4,5}, E. Pagot^{2,6}, P. Cloetens², F. Peyrin^{1,2}

¹ Université de Lyon, CREATIS-LRMN ; CNRS UMR5220 ; Inserm U630 ; INSA-Lyon ; Université Lyon 1, F69621 Villeurbanne, France

² European Synchrotron Radiation Facility, 6 rue Jules Horowitz, F38043 Grenoble, France

³ Julius Wolff Institut & Berlin-Brandenburg School for Regenerative Therapies, Charité - Universitätsmedizin Berlin Augustenburger Platz 1, 13353 Berlin, Germany

⁴ IPHEP, CNRS UMR 6046, UFR SFA, Université de Poitiers, 40 avenue du Recteur Pineau, F86022 Poitiers, France

⁵ CNPS, CNRS UMR 8620, Université Paris-Sud, F91405 Orsay, France

⁶ Current address: Nev@ntropic SAS, 16 bis rue du 14 Juillet, 97300 Cayenne, French Guiana

In this chapter, we describe X-ray phase tomography based on in-line phase contrast images. Phase tomography is a computational imaging technique, which is gaining increased attention due to the increase in sensitivity it offers over conventional, attenuation-based techniques. The increased sensitivity is of particular interest in biomedical imaging, especially for soft tissue visualization and analysis. The in-line technique offers a very simple imaging setup compared to other currently available X-ray phase contrast imaging techniques. The basic principles of the imaging technique are described, starting with an analysis of the image formation process, followed by a review of the most common reconstruction algorithms and practical results on parameter selection. Finally, three examples of biomedical imaging applications are presented: imaging of a human breast biopsy, small animal imaging and bone tissue engineering, with the aim to show imaging in different conditions and different reconstruction options.

Keywords X-ray microscopy; synchrotron radiation; phase contrast; phase retrieval; tomography; biomedical imaging

1. Introduction

In-line X-ray phase tomography is a computational imaging technique that relies on using the X-ray phase, calculated from Fresnel diffraction patterns, as input to a tomographic reconstruction algorithm to reconstruct the 3D refractive index distribution in a sample. Unlike attenuation, phase shift cannot be detected directly, but instead has to be put in evidence by introducing interference phenomena, known as phase contrast imaging. In the hard X-ray range, the from visible light microscopy well known technique of Zernike phase contrast [1], is unavailable with a large field of view due to the difficulty of producing the required X-ray optics. Nevertheless, several ways to achieve phase contrast in the hard X-ray range have been developed; essentially interferometry based [2, 3, 4], analyser-based [5] and propagation based [6, 7, 8]. All these techniques require that the beam used for imaging has a defined phase, i.e. that it has a high degree of coherence. Currently, the best sources of coherent X-rays for phase tomography are synchrotrons. While all of the mentioned techniques provide powerful phase contrast imaging, the main advantages of the propagation technique is its simple imaging setup, essentially the standard synchrotron radiation micro-computed tomography (SR- μ CT) setup [9] with the detector on a translation stage (Fig. 1), and that it introduces no optical elements in the beam path, effectively using all the available flux [8] and preserving the highest spatial resolution.

The main interest in phase imaging is the improved sensitivity it offers compared to attenuation-based techniques. The gain in sensitivity in the hard X-ray range can be several orders of magnitude for soft materials, which makes it appealing for biomedical imaging of soft tissue. Its main inconvenience is the need to calculate the phase shift, a process known as phase retrieval. Phase retrieval from Fresnel diffraction patterns is a non-linear inverse problem. So far, algorithms have depended on linearization of the forward problem, at first under the assumption of short propagation distances [10] or weak absorption [11]. Indeed, in the first application of this technique in biomedicine, imaging of a human breast biopsy, detailed in section 4, the samples were close to pure phase objects. In many biomedical imaging applications, however, there are also absorbing structures present. Essentially, four different cases can be distinguished:

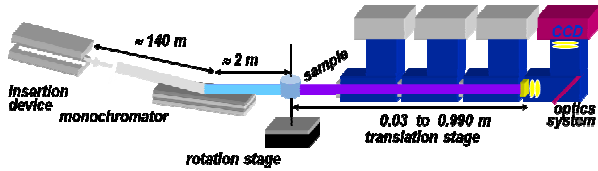


Fig. 1 The imaging setup of synchrotron radiation propagation-based phase contrast imaging. X-rays are taken from an insertion device, then monochromatized. The long source to sample distance yields a high degree of spatial coherence. The sample is mounted on a translation-rotation stage (standard SR- μ CT setup). The detector, consisting of a scintillator, light microscope optics and a CCD, is mounted on a translation stage to allow for free space propagation of the beam after the sample.

1. Weak absorption contrast. This case is common in e.g. biological imaging, where the sample might consist only of soft tissue.
2. Mostly weakly absorbing structures, in the presence of strongly absorbing ones. This case is common in e.g. medical applications and small animal imaging, where there can be a large range of absorption contrast between bone and soft tissue.
3. Mostly strongly absorbing structures with some soft ones. This case appears in e.g. bone research, where it might be desirable to resolve both bone microstructure and vascularization simultaneously.
4. Strongly absorbing structures with small relative absorption contrast. This case is common in e.g. paleontology, where the aim is to image small differences in mineralization in a fossil, and in materials science, where the aim might be to resolve grains of similar composition in an alloy.

Recently, phase tomography has been applied for strongly absorbing objects. Mainly two developments has made this possible: extension of the phase retrieval algorithms to the strong absorption case [12] and introduction of regularization techniques to deal with low frequency noise that often appear in the reconstructed refractive index when absorption is strong [13]. So far, in-line phase tomography is the only phase tomography technique that has been applied to the case of mixed soft/hard tissue samples. In this chapter, we describe the fundamentals of X-ray in-line phase contrast imaging. We further present reconstruction algorithms for both the weak and strong absorption case, and show three applications in biology, corresponding to case 1-3 above.

2. Propagation-based phase contrast imaging

In in-line, or propagation based, phase contrast imaging, phase contrast is achieved by simply letting the x-ray beam propagate in free space after interaction with the object. The contrast formation process can be understood in the framework of Fresnel diffraction.

2.1 Wave-object interaction

When an X-ray beam passes through an object, it may be affected in two ways: it might be absorbed in the object, which changes its amplitude, and it might be retarded in the object, which changes its phase. For X-rays we can consider the object completely described by the complex refractive index $n = \epsilon + i\beta$. Since ϵ is smaller than, but close to, unity for hard X-rays, the 3D complex refractive index distribution in the object can be written as

$$n(x, y, z) = 1 - \delta_n(x, y, z) + i\beta(x, y, z), \quad (1)$$

where δ_n is the complex refractive index decrement, β is the attenuation index and (x, y, z) the spatial coordinates. Both quantities δ_n and β are real and positive. The amplitude and phase modulations introduced on the incident wave by the object can be described by a transmittance function [14]

$$u_0(\mathbf{x}) = T(\mathbf{x})u_{inc}(\mathbf{x}) \quad (2)$$

where $u_{inc}(\mathbf{x})$ is the incident wave field, $u_0(\mathbf{x})$ the wave field at the exit plane of the object ($D=0$), $\mathbf{x}=(x,y)$ are the spatial coordinates in the plane perpendicular to the propagation direction z , and

$$T(\mathbf{x}) = A(\mathbf{x}) \exp[i\varphi(\mathbf{x})] = \exp[-B(\mathbf{x})] \exp[i\varphi(\mathbf{x})]. \quad (3)$$

Both the attenuation and the phase shift induced by the object can be described as projections through the absorption and refractive index distributions respectively, with

$$B(\mathbf{x}) = \left(\frac{2\pi}{\lambda}\right) \int \beta(x, y, z) dz \quad (4)$$

and

$$\varphi(\mathbf{x}) = -\left(\frac{2\pi}{\lambda}\right) \int \delta_n(x, y, z) dz. \quad (5)$$

This means that both parts of the complex refractive index can be reconstructed by tomographic reconstruction if amplitude and phase can be measured for different angular settings of the sample.

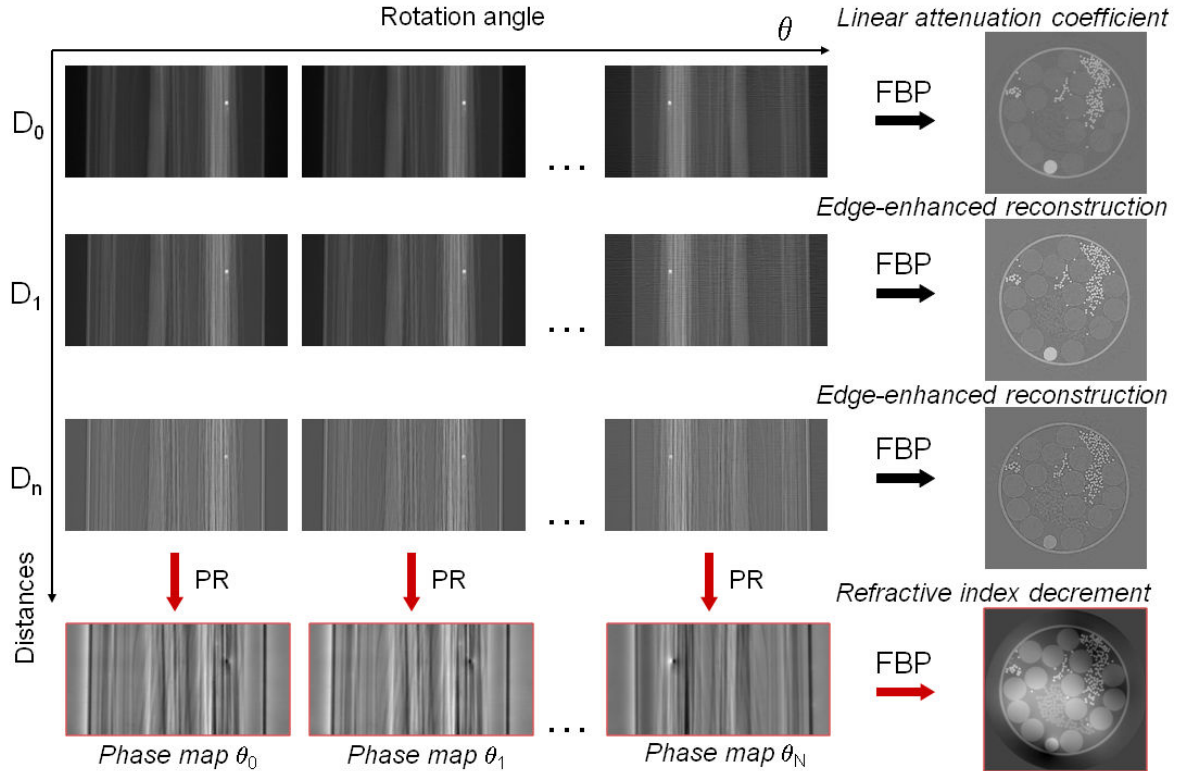


Fig. 2 Summary of the imaging modes available in the propagation based phase contrast setup. The first line illustrates standard tomographic acquisition: the projections of the samples for different angles of rotation are acquired with the detector close to the sample ($D \sim 0$). These radiographs are processed with the filtered back projection (FBP) algorithm to a reconstruction of the 3D absorption index. The second and third lines illustrate in-line *phase contrast tomography*. The tomographic acquisition is performed with the detector a distance ($D_1 \dots D_n$) from the sample. In this case the application of the standard FBP algorithm yields an edge-enhancement effect, which is proportional to the Laplacian of the refractive index. The fourth line illustrates in-line *phase tomography*. For each rotation angle, a phase retrieval (PR) algorithm is applied to the radiographs taken at different distances, providing the phase projection, or *phase map*. These reconstructed phase maps are then processed with the FBP algorithm to recover the 3D refractive index decrement.

2.2 Contrast formation

For the relatively short propagation distances we are interested in here, usually up to 1 m, the effect of propagation on the exit wave-field can be described in the framework of Fresnel diffraction. The wave field $u_D(\mathbf{x})$ at propagation distance D downstream of the object is then written [15]

$$u_D(\mathbf{x}) = \frac{\exp(ikD)}{i\lambda D} \iint u_0(\mathbf{x}_0) \exp\left\{i\frac{\pi}{\lambda D}[(x-x_0)^2 + (y-y_0)^2]\right\} d\mathbf{x}_0 \quad (6)$$

which is known as the Fresnel integral in the paraxial approximation (small diffraction angles). We can see that the effect of free space propagation on the wave-field is described by a linear system: we can identify Eq. 6 as a convolution integral. Written as a convolution we thus have

$$u_D(\mathbf{x}) = P_D(\mathbf{x}) * u_0(\mathbf{x}), \quad (7)$$

where

$$P_D(\mathbf{x}) = \frac{1}{i\lambda D} \exp\left(i\frac{\pi}{\lambda D} |\mathbf{x}|^2\right), \quad (8)$$

which is known as the Fresnel propagator. In many cases, for example for simulating phase contrast images, it is more convenient to describe this system in the Fourier domain, which is trivial since it is a linear system. The convolution in Eq. 7 then becomes a multiplication, and it turns out that the Fourier transform of the propagator can be written analytically. If we take the 2D Fourier transform as

$$\tilde{g}(\mathbf{f}) = \mathcal{F}\{g\}(\mathbf{f}) = \int g(\mathbf{x}) \exp(-i2\pi\mathbf{x} \cdot \mathbf{f}) d\mathbf{x}, \quad (9)$$

the Fourier transform of Eq. 8 is

$$\tilde{P}_D(\mathbf{f}) = \exp(-i\pi\lambda D|\mathbf{f}|^2). \quad (10)$$

The intensity of the wave at a distance D downstream of the sample is

$$I_D(\mathbf{x}) = |u_D(\mathbf{x})|^2, \quad (11)$$

which is the quantity that can be detected. Such an image is referred to as a Fresnel diffraction pattern or a phase contrast image. Intensity is measurable in essentially every plane downstream of the object, but the phase shift is lost, and has to be reconstructed from intensity images. There is thus a quantitative but non-linear relationship between the induced phase and the contrast.

2.3 Phase-contrast tomography

The phase contrast images can be used directly as input to a tomographic reconstruction algorithm. This yields an edge-enhancement effect which can already provide useful images, especially for soft tissue visualization. To show how the resulting contrast relates to the refractive index decrement, we start by observing that the intensity at distance D can be approximated as [8]

$$I_D(\mathbf{x}) \approx I_0(\mathbf{x}) \exp\left[-\frac{\lambda D}{2\pi} \nabla^2 \varphi(\mathbf{x})\right], \quad (12)$$

assuming that the absorption modulation $B(\mathbf{x})$ varies slowly compared to the phase modulation $\varphi(\mathbf{x})$. Taking the natural logarithm of Eq. 12, analogously to the pure absorption case, yields a projection of the form

$$-\ln[I_D(\mathbf{x})] \approx (4\pi/\lambda) \int \beta(x, y, z) dz - D \left(\frac{\partial^2}{\partial x^2} + \frac{\partial^2}{\partial y^2} \right) \int \delta_n(x, y, z) dz. \quad (13)$$

Since tomographic reconstruction is a linear operation, we can consider the two terms independently. The first term is simply the projection through the absorption index, as in Eq. 4. The second term is the 2D Laplacian in the image plane of the refractive index decrement projection. Using this as input to a tomographic reconstruction algorithm reconstructs

$$g(x, y, z) \approx (4\pi/\lambda) \beta(x, y, z) + D \left(\frac{\partial^2}{\partial x^2} + \frac{\partial^2}{\partial y^2} + \frac{\partial^2}{\partial z^2} \right) \delta_n(x, y, z), \quad (14)$$

which is the superposition of the linear attenuation coefficient $\mu(x, y, z) = (4\pi/\lambda) \beta(x, y, z)$ and the 3D Laplacian of the refractive index decrement. Note that this relation is an approximation valid for relatively short distances and weak phase.

3. Phase retrieval

More interesting is to use the quantitative relationship of Eq. 11 to reconstruct the phase shift from phase contrast images. It is not straight forward to use this relation directly, due to the non-linearity. Iterative methods, like those used in coherent diffraction imaging [16-20], could be considered, but are time consuming, do not guarantee convergence, and first applications have not been promising [21]. Instead, most reported methods can be considered as being based on linearization of Eq. 11 to provide a linear forward problem, which yields efficient reconstruction algorithms. Two main classes of algorithms can be identified in literature: algorithms based on a linearization with respect to the propagation distance, which yields what is known as the transport of intensity equation (TIE) [22-23], and algorithms based on linearization with respect to the object, which yields the contrast transfer function [11]. To derive the algorithms, it is useful to start from the observation that the Fourier transform of the recorded intensity can be written as [24]

$$\tilde{I}_D(\mathbf{f}) = \int T\left(\mathbf{x} - \frac{\lambda D \mathbf{f}}{2}\right) T^*\left(\mathbf{x} + \frac{\lambda D \mathbf{f}}{2}\right) \exp(-i2\pi\mathbf{x} \cdot \mathbf{f}) d\mathbf{x}. \quad (15)$$

3.1 Weak absorption case

If the absorption can be considered weak, we can Taylor expand to the first order with respect to the absorption and phase shift in Eq. 3 [11]:

$$T(\mathbf{x}) \approx 1 - B(\mathbf{x}) + i\varphi(\mathbf{x}). \quad (16)$$

Substituting into (Eq. 15) and retaining only first order terms yields a linear contrast model:

$$\tilde{I}_D^{CTF}(\mathbf{f}) \approx \delta(\mathbf{f}) - 2 \cos(\pi\lambda D|\mathbf{f}|^2)\tilde{B}(\mathbf{x}) + 2 \sin(\pi\lambda D|\mathbf{f}|^2)\tilde{\varphi}(\mathbf{x}), \quad (17)$$

where $\delta(\mathbf{f})$ is the 2D Dirac delta. Eq. 17 is known as the contrast transfer function. In spite of the initial assumption of weak absorption and phase, it is valid for weak absorption and slowly varying phase [24]:

$$B(\mathbf{x}) \ll 1, \quad |\varphi(\mathbf{x}) - \varphi(\mathbf{x} + \lambda D\mathbf{f})| \ll 1, \quad (18)$$

which is a weaker condition. Eq. 17 can be used to solve for both the absorption and phase by linear least squares optimization:

$$\arg \min_{\tilde{B}(\mathbf{x}), \tilde{\varphi}(\mathbf{x})} \sum_D \|\tilde{I}_D^{CTF}(\mathbf{f}) - \tilde{I}_D^{rec}(\mathbf{f})\|^2 + \alpha \|\tilde{\varphi}(\mathbf{x})\|^2 \quad (19)$$

where $\tilde{I}_D^{rec}(\mathbf{f})$ are the recorded intensity images and the second term is a regularization term [25] that prevents the solution from becoming unbounded. The solution for the phase is

$$\tilde{\varphi}(\mathbf{x}) = \frac{1}{2\Delta + \alpha} [A \sum_D \sin(\pi\lambda D|\mathbf{f}|^2)\tilde{I}_D^{rec}(\mathbf{f}) - B \sum_D \cos(\pi\lambda D|\mathbf{f}|^2)\tilde{I}_D^{rec}(\mathbf{f})], \quad (20)$$

where $A = \sum_D \sin(\pi\lambda D|\mathbf{f}|^2)\cos(\pi\lambda D|\mathbf{f}|^2)$, $B = \sum_D \cos^2(\pi\lambda D|\mathbf{f}|^2)$ and $\Delta = BC - A^2$ with $C = \sum_D \sin^2(\pi\lambda D|\mathbf{f}|^2)$. Due to the sine squared in the denominator in Eq. 20, the propagation distances have to be selected carefully to avoid zeros. The optimal distances have been found to be dependent on the pixel size p_s , wavelength and number of distances chosen (usually 2-4). It turns out that the optimal set of distances is always a combination of distances described by [26]

$$D = [k(c_2 p_s^2 + c_1 p_s + c_0) - d_1 p_s + d_0]/\lambda \quad (21)$$

with $c_0 = -5.3$, $c_1 = 0.4$, $c_2 = 38.4$, $d_0 = 4.67$, $d_1 = 13.3$, λ in Å, D in mm and $k \in \mathbb{N}$. The optimal values of k are (3, 5), (4, 5, 7) and (4, 6, 7, 9) for the most commonly used number of distances [26]. The possibility to use several propagation distances is an advantage since it allows to increase the signal to noise ratio by recording more phase information. A weakness of this model is that it is only valid when the absorption is weak. Reconstruction often retains the main features of the imaged object, but reconstructed values are underestimated [27]. Certain modifications have to be made to extend validity to the strong absorption case. To introduce these, we start by describing the transport of intensity model.

3.2 Short propagation distance case

The TIE describes the change induced in the wavefield by propagation over an infinitesimal distance. One possible way of deriving the TIE is to Taylor expand the transmittance function to the first order with respect to D in Eq. 11 as $T(\mathbf{x} + \lambda D\mathbf{f}/2) \approx T(\mathbf{x}) + \frac{1}{2}\lambda D\mathbf{f} \cdot \nabla T(\mathbf{x})$ [28], which yields

$$\frac{I_D(\mathbf{x}) - I_0(\mathbf{x})}{D} = -\frac{\lambda}{2\pi} \nabla \cdot [I_0(\mathbf{x})\nabla\varphi(\mathbf{x})]. \quad (22)$$

The Taylor expansion imposes that D must be small. If we let D go to zero, the left hand side of Eq. 22 can be identified as a differential so that

$$\frac{\partial}{\partial z} I_0(\mathbf{x}) = -\frac{\lambda}{2\pi} \nabla \cdot [I_0(\mathbf{x})\nabla\varphi(\mathbf{x})], \quad (23)$$

which is the transport of intensity equation [29]. Solving Eq 22 for the phase yields an elegant and efficient phase retrieval algorithm:

$$\varphi(\mathbf{x}) = -\frac{2\pi}{\lambda} \nabla^{-2} \left(\nabla \cdot \left\{ \frac{1}{I_0(\mathbf{x})} \nabla \left[\nabla^{-2} \frac{I_D(\mathbf{x}) - I_0(\mathbf{x})}{D} \right] \right\} \right), \quad (24)$$

provided that the inverse Laplacian is regularized, e.g. by using $\nabla^{-2} = (1/4\pi^2) \mathcal{F}^{-1} 1/(f_x^2 + f_y^2 + \alpha) \mathcal{F}$ [30]. Use of this algorithm in applied work has not been reported, however. This might be due to a susceptibility to low frequency noise (which is true for all algorithms for this problem, due to a weak transfer of information from phase shift to contrast in the low frequency range), and sensitivity to high frequency noise [27].

Several extensions to this algorithm have been reported, mainly with an eye to do phase retrieval from one phase contrast image only. With weak, or homogeneous, absorption, Eq. 24 becomes [31]

$$\varphi(\mathbf{x}) = -\frac{2\pi}{\lambda D} \nabla^{-2} \left(\frac{I_D(\mathbf{x})}{I_0(\mathbf{x})} - 1 \right), \quad (25)$$

which has been demonstrated to be a feasible algorithm in the weak absorption case, provided the regularizing parameter α is chosen properly [32]. This type of algorithm has found application where absorption is weak and close to homogeneous in e.g., imaging of microfossils [33]. Another proposition is to assume that the object is homogeneous, i.e. that the ratio δ_n/β is constant in the sample. Due to the homogeneity assumption, we can set $I_0(\mathbf{x}) = \exp[(2\beta/\delta_n)\varphi(\mathbf{x})]$ and rewrite Eq. 22 as [34]

$$\exp\left[\frac{2\beta}{\delta_n}\varphi(\mathbf{x})\right] = I_D(\mathbf{x})\left(-\frac{\lambda D}{2\pi}\frac{\delta_n}{2\beta}\nabla^2 + 1\right)^{-1}. \quad (26)$$

We can solve Eq. 26 for the phase as [34]

$$\varphi(\mathbf{x}) = \frac{\delta_n}{2\beta}\left[\ln\mathcal{F}^{-1}\left\{\frac{I_D}{\frac{\lambda D}{2\pi}\frac{\delta_n}{2\beta}|\mathbf{f}|^2+1}\right\}(\mathbf{x})\right], \quad (27)$$

Which, like Eq. 25, only requires one image, but has yet to be proven experimentally in an applied study.

3.3 Strong absorption case

To take into account strong absorption, the linearization of Eq. 11 can be modified to a linearization with respect to the phase only in a first step, which yields [12]

$$\tilde{I}_D(\mathbf{f}) = \int A\left(\mathbf{x} - \frac{\lambda D\mathbf{f}}{2}\right)A\left(\mathbf{x} + \frac{\lambda D\mathbf{f}}{2}\right)\left[1 + i\varphi\left(\mathbf{x} - \frac{\lambda D\mathbf{f}}{2}\right) - i\varphi\left(\mathbf{x} + \frac{\lambda D\mathbf{f}}{2}\right)\right]\exp(-i2\pi\mathbf{x}\cdot\mathbf{f})d\mathbf{x}. \quad (28)$$

Expanding the multiplication and making the variable changes $\mathbf{y} = \mathbf{x} + \lambda D\mathbf{f}/2$ and $\mathbf{y} = \mathbf{x} - \lambda D\mathbf{f}/2$ gives

$$\begin{aligned} \tilde{I}_D(\mathbf{f}) &= \tilde{I}_D^{\varphi=0}(\mathbf{f}) + \sin(\pi\lambda D|\mathbf{f}|^2)\int A(\mathbf{x})\varphi(\mathbf{x})[A(\mathbf{x} + \lambda D\mathbf{f}) + A(\mathbf{x} - \lambda D\mathbf{f})]\exp(-i2\pi\mathbf{x}\cdot\mathbf{f})d\mathbf{x} \\ &+ i\cos(\pi\lambda D|\mathbf{f}|^2)\int A(\mathbf{x})\varphi(\mathbf{x})[A(\mathbf{x} + \lambda D\mathbf{f}) - A(\mathbf{x} - \lambda D\mathbf{f})]\exp(-i2\pi\mathbf{x}\cdot\mathbf{f})d\mathbf{x}, \end{aligned} \quad (29)$$

where $\tilde{I}_D^{\varphi=0}(\mathbf{f})$ is the intensity if there was no phase shift. This is usually approximated by the Fourier transform of the absorption image i.e., $\tilde{I}_0(\mathbf{f})$. At this stage, a linearization with respect to the absorption is introduced, with $A(\mathbf{x} + \lambda D\mathbf{f}) + A(\mathbf{x} - \lambda D\mathbf{f}) \approx 2A(\mathbf{x})$ and $A(\mathbf{x} + \lambda D\mathbf{f}) - A(\mathbf{x} - \lambda D\mathbf{f}) \approx 2\lambda D\mathbf{f}\cdot\nabla A(\mathbf{x})$ (under the condition that the absorption is slowly varying i.e., $|B(\mathbf{x} + \lambda D\mathbf{f}) - B(\mathbf{x} - \lambda D\mathbf{f})| \ll 1$). The resulting integrals can be identified as Fourier transforms, so we have the linear contrast model

$$\tilde{I}_D^{MIX}(\mathbf{f}) = \tilde{I}_D^{\varphi=0}(\mathbf{f}) + 2\sin(\pi\lambda D|\mathbf{f}|^2)\mathcal{F}\{I_0\varphi\}(\mathbf{f}) + \cos(\pi\lambda D|\mathbf{f}|^2)\frac{\lambda D}{2\pi}\mathcal{F}\{\nabla\cdot(\varphi\nabla I_0)\}(\mathbf{f}). \quad (30)$$

This formula has the advantage of being valid for strong absorption. It also unifies the CTF and TIE as it approaches the TIE in the limit of short propagation distance, and the CTF in the limit of weak absorption. Eq. 30 can, similarly to Eq. 17, be used to pose a linear least squares minimization problem. However, due to the derivatives of the phase appearing in the third term, this is solved by successive minimizations and updates of the phase gradient. It is also more convenient to solve for the phase-absorption product $\psi(\mathbf{x}) = I_0(\mathbf{x})\varphi(\mathbf{x})$ that appears in the second term. We therefore have

$$\tilde{\psi}^{(n+1)}(\mathbf{f}) = \frac{\sum_D C_D(\mathbf{f})[\tilde{I}_D(\mathbf{f}) - \tilde{I}_D^{\varphi=0}(\mathbf{f}) - \Pi_D^{(n)}(\mathbf{f})]}{\sum_D C_D^2(\mathbf{f}) + \alpha}, \quad (31)$$

with $C_D(\mathbf{f}) = 2\sin(\pi\lambda D|\mathbf{f}|^2)$ and $\Pi_D^{(n)}(\mathbf{f}) = \cos(\pi\lambda D|\mathbf{f}|^2)\frac{\lambda D}{2\pi}\mathcal{F}\{\nabla\cdot[\psi^{(n)}\nabla\ln(I_0)]\}(\mathbf{f})$ where $\psi^{(0)}(\mathbf{x}) = 0$. The phase can then be found by dividing away the absorption image.

3.4 Regularization of phase retrieval

Sometimes, the reconstructed refractive index shows strong low-frequency noise, as shown in the refractive index decrement reconstruction in Fig. 2. This can strongly inhibit the possibility to quantitatively analyze the reconstructed volumes. This kind of artefact can be handled by introducing information in the low frequency range from the measured attenuation. By assuming that the object is homogeneous i.e., that the ratio δ_n/β is constant, we can define an *a priori* term on the low frequencies [13]:

$$\tilde{\psi}_0(\mathbf{f}) = H(\mathbf{f})\mathcal{F}\left\{\frac{\delta}{2\beta}I_0\ln(I_0)\right\}(\mathbf{f}), \quad (32)$$

where $H(\mathbf{f})$ is a suitably chosen low-pass filter. Eq. 31 then becomes

$$\tilde{\psi}^{(n+1)}(\mathbf{f}) = \frac{\sum_D C_D(\mathbf{f})[\tilde{I}_D(\mathbf{f}) - \tilde{I}_D^{\varphi=0}(\mathbf{f}) - \Pi_D^{(n)}(\mathbf{f})] + \alpha\tilde{\psi}_0(\mathbf{f})}{\sum_D C_D^2(\mathbf{f}) + \alpha}. \quad (33)$$

The parameter α can be chosen with the L-curve criterion [13, 35]. This is defined as the parametric curve $c(\alpha) = [\log(|M(\alpha)|), \log(|R(\alpha)|)]$, where $M(\alpha)$ is the model error (e.g. with the mixed approach, $M(\alpha) = \sum_D |C_D(\mathbf{f})\tilde{\psi}_\alpha(\mathbf{f}) - [\tilde{I}_D(\mathbf{f}) - \tilde{I}_D^{\varphi=0}(\mathbf{f}) - \Pi_D(\mathbf{f})]|$), where $\tilde{\psi}_\alpha(\mathbf{f})$ is the solution for a certain value of α , and $R(\alpha) = |\tilde{\psi}_\alpha(\mathbf{f}) - \tilde{\psi}_0(\mathbf{f})|$ is the regularization error. The optimal value of α , in the sense that a change in α will make the minimal change to both error terms, i.e. the optimal trade off between the two error terms, is then found at the point of maximum curvature (the ‘‘corner’’) of the L-curve. A practical implementation is to sample the L-curve at a number of values of α , then fitting a cubic spline to these points, for which it is easy to find the point of maximum curvature [13].

3.5 Phase tomography

All the above mentioned phase retrieval algorithms can be coupled to a tomographic reconstruction algorithm such as FBP. Phase retrieval is then applied to the radiograph(s) recorded at different distances, separately for each angle. The phase maps are then used as input to the tomographic reconstruction algorithm (Fig. 2).

4. Applications

We now show three applications of phase tomography in biomedical imaging, based on data acquired on the ID19 beamline at the European Synchrotron Radiation Facility (ESRF). Even though there is not yet a large body of applied work with the presented techniques, the following applications have been chosen to present different imaging and reconstruction parameters.

The first application, imaging of a human breast biopsy [36], is an example of imaging of pure soft tissue samples and corresponds to the first case in section 1. This case can be extended to other types of samples involving imaging of soft tissues only.

In the second application, small animal imaging for soft tissue anatomy [37], a very small earless frog is imaged to elucidate the anatomy of its hearing apparatus. Due to the small size of the animal, this is a particularly challenging case of small animal imaging. This corresponds to the second case in section 1, and can be extended to anatomical imaging of other small animals, such as mice.

The third application, imaging of porous biomaterials for soft tissue quantification [38], corresponds to case 3 in section 1. Due to the strong absorption and mix of soft and hard tissues, this is the most challenging case. The imaging methodology could be extended to e.g. bone biopsies and high resolution imaging of small animal anatomy.

4.1 Imaging of a soft tissue biopsy

Conventional X-ray mammography, based on the absorption of X-rays in the tissues, remains the gold standard employed for breast cancer screening. However, about ten to twenty percent of the clinically evident breast cancers with palpable abnormalities are not detected by this technique. The potential interest of phase imaging in this context is two-fold: 1) better and earlier detection of anomalies and 2) screening cancer with a lower X-ray dose.

As a feasibility study [36], we performed phase tomography of small excised breast tissue samples obtained from biopsies. The biopsy was enclosed in a 13 mm diameter and 17 mm height container, made from 1 mm thick Plexiglas. It originates from a patient who suffers from chronic mastopathy. Mastopathy is a broadbenoma and cystic disease of the breast. It is characterized by an imbalance between epithelial and connective tissue growth with highly proliferative and regressive changes of the breast tissue. Although mastopathy is a benign disease, this pathology can be a temporary phase in the malignant tumour development process. In the lower part of the sample, skin tissue can be found. The rest of the sample contains adipose and glandular tissue. The skin was oriented perpendicular to the cylinder axis such that about 10 mm of tissue is projected onto the detector.

Figure 3 compares an absorption radiograph (a) and a retrieved phase map (b) of the cylinder containing the biopsy. The radiographs were acquired at an X-ray energy of 25 keV and a detector pixel size of 7.5 μm . The phase map as compared to the absorption image shows similar texture of the tissue but with a clear enhancement of contrast. In order to optimize the contrast for soft tissues at relatively low spatial resolution, very large propagation distances were used: 0.03 m (attenuation), 1 m, 4.3 m and 8.8 m. The phase map was retrieved assuming a slowly varying phase and no amplitude modulation. In order to account for the attenuation that necessarily occurs in the relatively thick sample, the contribution of attenuation was eliminated by division with the absorption image. This is a usable ad hoc solution if the absorption introduces a slowly

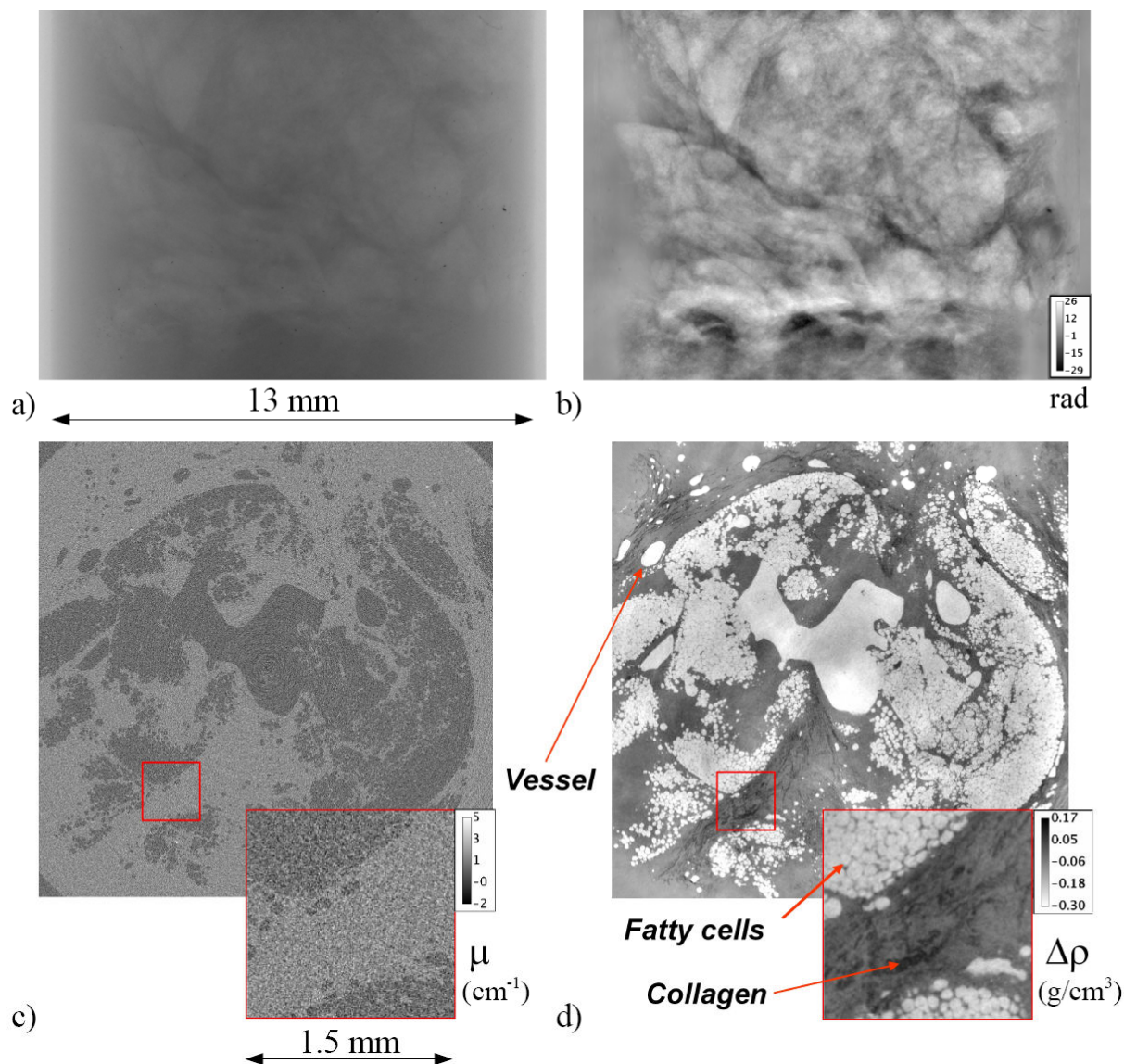


Fig. 3 Comparison of attenuation and phase imaging of a human breast biopsy. (a) Absorption image recorded at 0.03 m sample-to-detector distance. (b) Phase map retrieved from 4 propagation based images recorded at 0.03 m, 1 m, 4.3 m and 8.8 m. (c) Tomographic slice mapping the linear attenuation coefficient in the breast tissues. (d) Tomographic slice mapping the variations of the mass density in the breast tissues. The contrast is inverted with respect to the attenuation case. The magnified portion in (d) clearly reveals the collagen and fatty cells.

varying envelope in the signal. In more complex cases, the mixed approach as described by Eq. 30-31 is required. Due to the large propagation distances used (up to 8.8 m) and despite the very large source-to-sample distance of 145 m on beamline ID19, a significant magnification of the radiographs occurs. The images were corrected for this magnification before the actual phase retrieval.

In order to obtain three-dimensional images, this procedure was repeated for 1200 angular positions of the sample. Fig. 3 (c) and (d) show tomography sections of the biopsy. The slice chosen corresponds to the center of the sample. The phase tomography (Fig. 3 (d)) shows a big improvement of the contrast compared to the absorption tomography (Fig. 3 (c)) and greatly facilitates feature characterization. Many details hardly perceptible in the absorption mode, such as fatty cells and collagen fibrils, are clearly distinguishable due to the increased contrast. For the phase tomography, the grayscale in the images scales linearly with the density of the tissues. Dark regions represent denser materials (smaller refractive index). The fatty cells (bright regions) appear with a lower density than the matrix (formalin) and than the collagen fibrils which are packed, forming bundles (dark regions). Phase tomography provides 3D density maps that are qualitatively very similar to histological sections, taken with the same resolution. This could represent an advantage for the characterisation of biopsies, enabling the bulk of the sample to be rapidly examined and avoiding the constraints and artefacts related to the sample preparation for histology.

4.2 Small animal imaging for soft tissue anatomy

Brachycephalus didactyla, one of the world's smallest tetrapods (9.8 mm SVL for a mature adult male), lacks an external tympanum [39]. The lack of a tympanum is one of the most common anatomical modifications in anurans [40-41] and is manifested in its most extreme form (in about 6% of the world's species) by the complete absence of a middle ear (tympanum, tympanal ring, columella, extracolumella, middle ear cavity, and eustachian tube). Without the external tympanum acting as an interface between the external environment and the inner ear, this species can be considered anatomically deaf. Paradoxically, species of the genus *Brachycephalus* still display acoustic behavior. Even though a relatively large number of species without a middle ear are known, the origins of earless frog are still unclear, largely due to their complex nature [42]. A detailed knowledge of the 3D structure and composition of the ear is crucial to clarify the functioning and evolution of the hearing mechanism.

A frog specimen (adult *B. didactyla*, specimen collection of the Museum National d'Histoire Naturelle (MNHN) collected in Southeastern Brazil, close to Rio de Janeiro, in 1970) was placed in a small polypropylene tube, filled with a 1 % formalin solution, for imaging. Images were obtained using 35 KeV wiggler radiation monochromatized with a vertical double Si-crystal monochromator [43-44]. A FReLoN CCD Camera [45] was used for detection, with an image size of 2048 x 2048 pixels at a pixel size of 4.91 μm . Three sample-detector distances (0.04, 0.5 and 0.9 m) were used, at which 1000 radiographic images were acquired over a 180° range. Phase retrieval was performed using the mixed approach (Eq. 30-31), and the 3D refractive index distribution was reconstructed using FBP. From this the 3D skull structure and soft tissue details were extracted. Three dimensional renderings were obtained after semi-automatic segmentation of the skeleton, using Avizo 6.1 (Mercury Computer Systems, Chelmsford, MA, USA)

Comparing absorption and phase tomography, it is clear that soft tissue visualization is enhanced in the phase tomography (Fig. 4 (a-b)). The phase tomography enables segmentation and visualization of both mineralized and non-mineralized tissue (Fig. 4 (c)). Based on the phase tomography data, it is possible to show that *B. didactyla* has a middle ear consisting of only an operculum and an opercular muscle. The operculum is partially ossified, contrary to what is observed in anurans with a middle ear (Fig. 4 (d)). The analysis of the phase tomography data shows a well developed sensorial papilla and the presence of cartilage inside the interstitial space of the otic capsule.

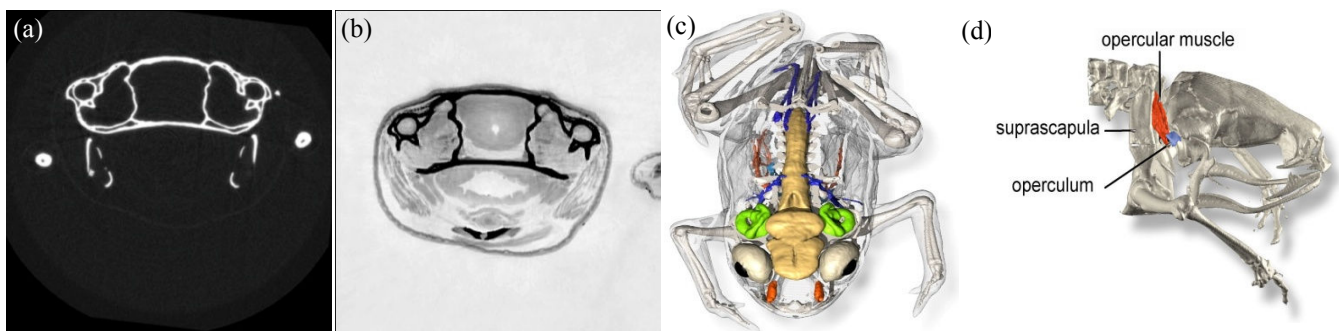


Fig. 4 Slices from (a) SR- μ CT, and (b) phase tomography. In (a), contrast in the mineralized tissue is good, but soft tissue is almost invisible. In (b), both soft and hard tissue is well contrasted. From this reconstruction it is possible to segment and visualize bones, organs and parts of the central and peripheral nervous systems (c). This permits detailed anatomical study of the hearing apparatus in the specimen, such as segmentation of the operculum and opercular muscle (d).

4.3 Imaging of porous biomaterials for soft tissue quantification

The use of biodegradable, porous biomaterials in conjunction with tissue engineering techniques shows promise for use as artificial bone grafts [46], known as scaffolds. They can also be used as substrates for 3D cell cultures of e.g., bone forming cells, for the study of different culture conditions, the performance of different biomaterials, or the effect on cell behavior of environmental factors such as weightlessness. Desired properties of these biomaterials are that they have a surface favorable for cell attachment, that they stimulate osteoblast precursors to differentiate into mature bone forming cells, and that they can contribute to bone regeneration. They should also be resorbable by the receiving body, and be replaced by new, living bone [47]. Bone formation and resorption can be quantified by SR- μ CT [48] and microdiffraction [49], but these techniques lack the sensitivity to resolve the fibrous tissue. Quantification of this soft tissue is important for the characterization of such biomaterials, since it constitutes the sites where new bone formation is possible. Phase tomography, however, enables the analysis of this phase [38].

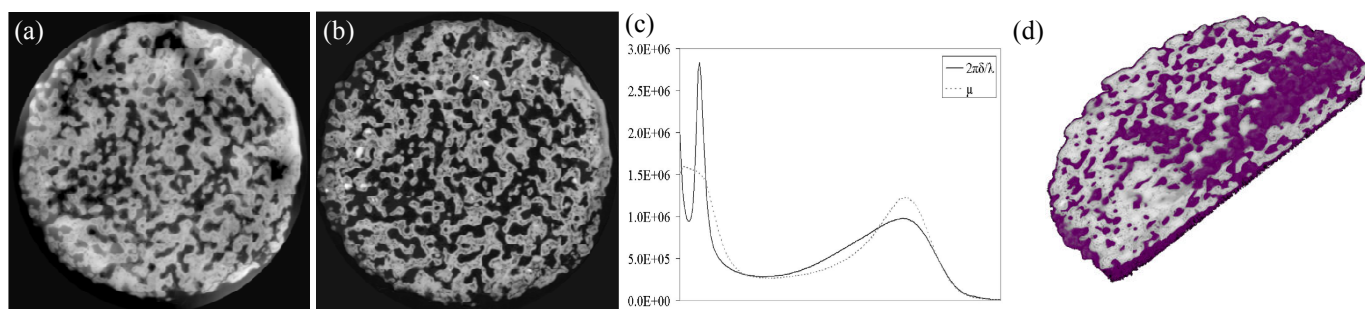


Fig. 5 Slices of (a) phase tomographic reconstruction without prior (Eq. 31) and (b) with prior (Eq. 33). The reconstruction in (a) shows strong low frequency artefacts. In the reconstruction with prior (b), the low frequency artefacts are alleviated. (c) Histogram of linear attenuation coefficient and refractive index, normalized to the same range. A peak corresponding to soft tissue is clearly visible in the refractive index histogram. (d) Soft and hard tissue can be segmented by thresholding. It can be seen that soft tissue is formed mainly inside the scaffold construct and that the volume filling fraction is high.

Discs of Skelite measuring 9 mm diameter and 1.2 mm thick, where seeded with osteoblast (OB) cells for 8 weeks, then washed in phosphate buffered saline (PBS), fixed in paraformaldehyde and stored in 70 % ethanol. Skelite is a bone graft substitute consisting of 67 % Silicon stabilized tricalcium phosphate (Si-TCP) and 33 % hydroxylapatite (HA). It has an open pore structure similar to human cancellous bone, with a pore size between 200 and 500 μm , and a porosity level around 60 % [50-51]. Samples were dried before imaging and mounted three and three in a Perspex cylinder, separated by fibre tissue paper and lightly compressed with a foam material, to take advantage of the 7 mm vertical field of view.

Imaging was performed using undulator radiation, monochromatized with a single Si crystal vertical reflection monochromator to 30 keV. The scintillator used was a 10 μm Gadox screen and detection was performed with a FreLoN camera [45] and standard light microscope optics, yielding a pixel size of 5 μm . The samples were strongly absorbing even at this energy, absorbing around 60 % of the X-rays at the thickest cross-section. Tomographic data sets were recorded over 2000 angles of view at 3 distances (0.01, 0.33, and 0.99 m), with an exposure time of 0.4 s. Phase retrieval was performed including the a priori term using (Eq. 32-33). The δ_n/β -ratio was set to correspond to the scaffold phase and was determined using the XOP software [52] to be $\delta_n/\beta = 380$. The regularizing parameter was set using the L-curve criterion (Section 3.4) to $\alpha = 10^{-3.21}$.

The reconstruction using no a priori knowledge (Eq. 30-31) showed strong low frequency artefacts, preventing a correct quantitative analysis (Fig. 5 (a)). These artefacts were alleviated by introducing the *a priori* term (Eq. 30, Fig. 5 (b)). This shows when the introduction of the homogeneity prior (Eq. 32) is called for, and illustrates its utility. Comparing the attenuation- and phase-based reconstructions (Fig. 5 (c)), it is clear that the phase tomography makes the soft tissue phase visible in the histogram. This enables segmentation, visualization (Fig. 5 (d)) and quantitative analysis (such as volume, volume filling fraction and local thickness) of the soft tissue phase. These types of measurements can be used to evaluate the osteoconductive and osteoinductive properties of different scaffold types, as well as the impact of different culture conditions, such as chemical environment and weightlessness.

5. Conclusion

The combination of phase retrieval from Fresnel diffraction patterns and tomographic imaging yields a highly sensitive 3D characterization technique that provides new insights in the imaging of both soft and hard tissue. The often huge amounts of data generated by the image acquisition scheme (typically in the range of 3000 2048 \times 2048 pixel projection images, taken at 2-4 distances in double precision, for a data set size of \sim 90-180 Gb) requires some care to be taken for data handling and implementation of the phase retrieval and tomographic reconstruction.

Future development of the technique is the adaptation towards higher resolutions than possible with a parallel beam setup, by using X-ray focusing optics, such as Kirkpatrick-Baez mirrors, to perform projection microscopy [53]. In this case, phase retrieval seems mandatory, since propagation distances will be relatively large, which goes beyond the edge detection regime of phase contrast tomography. Algorithms for the strong absorption case which do not assume the availability of an attenuation image will have to be developed. Another direction is the development of regularized methods that allow for heterogeneous objects. Current implementations assume that the imaged object is homogeneous, which often solves the intended problem (e.g. Fig. 5), at the cost of introducing new artefacts where the homogeneity assumption is not fulfilled.

A promising algorithm to combine reconstructions with different ratios has been proposed [54], which introduces an adaptation to multi-phase objects, but remains to be tested in an applied case.

This chapter was intended to give an introduction to phase tomography. Different examples were presented to show the potential of this technique in biomedical imaging. It was shown that phase tomography offers new possibilities for

visualization and quantification in a wide range of applications in biology and biomedicine, ranging from mammography to bone biology and small animal imaging.

Acknowledgements The authors would like to thank the ESRF for providing beam time for the imaging, R Cancedda, F. Tortelli and Y. Liu for work on the biomaterial samples. The breast biopsy was obtained from Marja-Liisa Karjalainen-Lindsberg, Helsinki University Central Hospital (HUCH), Finland, and we acknowledge the work of S. Fiedler, A. Bravin, P Coan, K. Fezzaa, J. Baruchel and J. Härtwig on imaging of the biopsy. We are grateful to A. Olier at the MNHN, Paris, for material kindly loaned from the MNHN collection).

References

- [1] Zernike F. Phase-contrast, a new method for microscopic observation of transparent objects. Part I. *Physica*. 1942;9:686-698.
- [2] Bonse U, Hart M. An X-ray interferometer. *Applied Physics Letters*. 1965;6:155-156.
- [3] Momose A, Takeda T, Itai Y, Hirano K. Phase-contrast X-ray computed tomography for observing biological soft tissues. *Nature Medicine*. 1996;2:473-475.
- [4] Weitkamp T, Nöhhammer B, Diaz A, David C, Ziegler E. X-ray wavefront analysis and optics characterization with a grating interferometer. *Applied Physics Letters*. 2005;86: 054101(3).
- [5] Chapman D, Thomlinson W, Johnston R E, Washburn D, Pisano E, Gmür N, Zhong Z, Menk R, Arfelli F, Sayers D. Diffraction enhanced X-ray imaging. *Physics in Medicine and Biology*. 1997;42:2015-2025.
- [6] Snigirev A, Snigireva I, Kohn V, Kuznetsov S, Schelokov I. On the possibilities of X-ray phase contrast microimaging by coherent high-energy synchrotron radiation. *Review of Scientific Instruments*. 1995;66:5486-5492.
- [7] Wilkins S W, Gureyev T E, Gao D, Pogany A, Stevenson A W. Phase-contrast imaging using polychromatic hard X-rays. *Nature (London)*. 1996;384:335-337.
- [8] Cloetens P, Pateyron-Salomé M, Buffière J, Peix G, Baruchel J, Peyrin F, Schlenker M. Observation of microstructure and damage in materials by phase sensitive radiography and tomography. *Journal of Applied Physics*. 1997;81:5878-5886.
- [9] Salomé M, Peyrin F, Cloetens P, Odet C, Laval-Jeantet A, Baruchel J, Spanne P. A synchrotron radiation microtomography system for the analysis of trabecular bone samples. *Medical Physics*. 1999;26:2194-2204.
- [10] Nugent K, Gureyev T, Cookson D, Paganin D, Barnea Z. Quantitative phase imaging using hard X-rays. *Physical Review Letters*. 1996;77:2961-2964.
- [11] Cloetens P, Ludwig W, Baruchel J, Van Dyck D, Van Landuyt J, Guigay J, Schlenker M. Holotomography: Quantitative phase tomography with micrometer resolution using hard synchrotron radiation X-rays. *Applied Physics Letters*. 1999;75:2912-2914.
- [12] Guigay J, Langer M, Boistel R, Cloetens P. A mixed contrast transfer and transport of intensity approach for phase retrieval in the Fresnel region. *Optics Letters*. 2007;32:1617-1619.
- [13] Langer M, Cloetens P, Peyrin F. Regularization of phase retrieval with phase-attenuation duality prior for 3D Holotomography. *IEEE Transactions on Image Processing*. 2010.
- [14] Goodman J W. *Introduction to Fourier optics*. 3rd ed. Greenwood Village, CO: Roberts; 2005.
- [15] Born M, Wolf E. *Principles of optics*. 7th ed. Cambridge, UK: Cambridge University Press; 1997.
- [16] Miao J, Charalambous P, Kirz J, Sayre D. Extending the methodology of X-ray crystallography to allow imaging of micrometer-sized non-crystalline specimens. *Nature*. 1999;400:342-344.
- [17] Marchesini S, Chapman H N, Hau-Riege S P, London R A, Szoke A, Me H, Howells M R, Padmore H, Rosen R, Spence J C H, Weierstall U. Coherent X-ray diffractive imaging: applications and limitations. *Optics Express*. 2003;11:2344-2353.
- [18] Gerchberg R W, Saxton W O. A Practical algorithm for the determination of phase from image and diffraction plane pictures. *Optik*. 1972;35:237-246.
- [19] Fienup J R. Phase retrieval algorithms: a comparison. *Applied Optics*. 1982;21:2758-2769.
- [20] Elser V. Phase retrieval by iterated projections. *Journal of the Optical Society of America A*. 2003;20:40-55.
- [21] Langer M. *Phase retrieval in the Fresnel region for hard X-ray tomography*. PhD Thesis. Villeurbanne, France: INSA-Lyon; 2008.
- [22] Teague, M R. Irradiance moments: their propagation and use for unique retrieval of phase. *Journal of the Optical Society of America* 1982;72:1199-1209
- [23] Teague, M R. Deterministic phase retrieval: a Green's function solution. *Journal of the Optical Society of America* 1982;73:1434-1441.
- [24] Guigay J. Fourier transform analysis of Fresnel diffraction patterns and in-line holograms. *Optik*. 1977;46:121-125.
- [25] Tikhonov A N, Arsenin V A. *Solution of ill-posed problems*. Washington DC: Winston; 1977.
- [26] Zabler S, Cloetens P, Guigay J, Baruchel J, Schlenker M. Optimization of phase contrast imaging using hard X-rays. *Review of Scientific Instruments*. 2005;76:073705(7p).
- [27] Langer M, Cloetens P, Guigay J, Peyrin F. Quantitative comparison of direct phase retrieval algorithms in in-line phase tomography. *Medical Physics*. 2008;35:4556-4566.
- [28] Turner L D, Dhal B B, Hayes J P, Nugent K A, Paterson D, Scholten R E, Tran C Q, Peele A G. X-ray phase imaging: demonstration of extended conditions with homogeneous objects. *Optics Express*. 2004;12:2960-2965.
- [29] Paganin D, Nugent K A. Noninterferometric phase imaging with partially coherent light. *Physical Review Letters*. 1998;80:2586-2589.
- [30] Paganin D M. *Coherent X-ray optics*. Oxford: Oxford University Press; 2006.
- [31] Bronnikov A V. Theory of quantitative phase-contrast computed tomography. *Journal of the Optical Society of America A*. 2002;19:472-480.
- [32] Groso A, Abela R, Stampanoni M. Implementation of a fast method for high resolution phase contrast tomography. *Optics Express*. 2006;14:8103-8110.

- [33] Friis E, Crane P, Pedersen K, Bengtsson S, Donoghue P, Grimm G, Stampanoni M. Phase-contrast X-ray microtomography links cretaceous seeds with gnetales and bennettitales. *Nature*. 2007;450:549-552.
- [34] Paganin D, Mayo S C, Gureyev T E, Miller P R, Wilkins S W. Simultaneous phase and amplitude extraction from a single defocused image of a homogeneous object. *Journal of Microscopy*. 2002;206:33-40.
- [35] Hansen P C, O'Leary D P. The use of the L-curve in the regularization of discrete ill-posed problems. *SIAM Journal on Scientific Computing*. 1993;14:1487-1503.
- [36] Pagot E, Fiedler S, Cloetens P, Bravin A, Coan P, Fezzaa K, Baruchel J, Härtwig J. Quantitative comparison between two phase contrast techniques: diffraction enhanced imaging and phase propagation imaging. *Physics in Medicine and Biology*. 2005;50:709-724.
- [37] Boistel R, Brigitte G, Cloetens P, Delzescaux T, Pollet N. Apport de la micro imagerie IRM et synchrotron pour l'étude de l'oreille du plus petit amphibien du monde *Psyllophryne didactyla*. *XI Congrès du GRAMM*. France: 2004:53(1p).
- [38] Langer M, Liu Y, Tortelli F, Cloetens P, Cancedda R, and Peyrin F. Regularized phase tomography enables study of mineralized and unmineralized tissue in porous bone scaffold. *Journal of Microscopy*. 2010;238:230-239.
- [39] Izecksohn E. Novo gênero e nova espécie de Brachycephalidae do Estado do Rio de Janeiro, Brasil (Amphibia, Anura). *Boletim do Museu Nacional. Nova Serie, Zoologia*. 1971;280:1-12.
- [40] Wever E G. The amphibian ear. Princeton: Princeton University Press; 1985.
- [41] Duellman W E, Trueb L. *Biology of Amphibians*. New York: McGraw-Hill; 1986.
- [42] Van der Meijden A, Boistel R, Gerlach J, Ohler A, Vences M, Meyer A. Molecular phylogenetic evidence for paraphyly of the genus *Sooglossus*, with the description of a new genus of Seychellean frogs. *Biological Journal of the Linnean Society*. 2007;91:347-359.
- [43] Betz O, Wegst U, Weide D, Heethoff M, Helfen L, Lee W K, Cloetens P. Imaging applications of synchrotron X-ray phase contrast microtomography in biological morphology and biomaterials science. I. General aspects of the technique and its advantages in the analysis of millimetre-sized arthropod structure. *Journal of Microscopy*. 2007;227:51-71.
- [44] Van der Meijden A, Boistel R, Gerlach J, Ohler A, Vences M, Meyer A. Molecular phylogenetic evidence for paraphyly of the genus *Sooglossus*, with the description of a new genus of Seychellean frogs. *Biological Journal of the Linnean Society*. 2007;91:347-359.
- [45] Labiche J, Mathon O, Pascarelli S, Newton M A, Ferre G G, Curfs C, Vaughan G, Homs A, Carreiras D F. The fast readout low noise camera as a versatile x-ray detector for time resolved dispersive extended x-ray absorption fine structure and diffraction studies of dynamic problems in materials science, chemistry, and catalysis. *Review of Scientific Instruments*. 2007;78:091301(11p).
- [46] Kofron MD, Li X, Laurencin C T. Protein- and gene-based tissue engineering in bone repair. *Current Opinion in Biotechnology*. 2004;15:399-405.
- [47] Glazer P A, Spencer U M, Alkalay R N, Schwarzt J. In vivo evaluation of calcium sulphate as a bone graft substitute for lumbar spine fusion. *The Spine Journal*. 2001;1:395-401.
- [48] Komlev V S, Peyrin F, Mastrogiacomo M, Cedola A, Papadimitropoulos A, Rustichelli F, Cancedda R. Kinetics of in vivo bone deposition by bone marrow stromal cells into porous calcium phosphate scaffolds: an X-ray computed microtomography study. *Tissue Engineering*. 2006;12:3449-3454.
- [49] Cancedda R, Cedola A, Giuliani A, Komlev V, Lagomarsino S, Mastrogiacomo M, Peyrin F, Rustichelli F. Bulk and interface investigations of scaffolds and tissue-engineered bones by X-ray microtomography and X-ray microdiffraction. *Biomaterials*. 2007;28:2505-2524.
- [50] Sayer M, Stratilatov A D, Reid J, Calderin L, Scott M J, Yin X, MacKenzie M, Smith T J N, Hendry J A, Langstaff S D. Structure and composition of silicon-stabilized tricalcium phosphate. *Biomaterials*. 2003;24:369-382.
- [51] Reid J W, Pietak A, Sayer M, Dunfield D, Smith T. Phase formation and evolution in the silicon substituted tricalcium phosphate/apatite system. *Biomaterials*. 2005;26:2887-2897.
- [52] Dejus R J, Sanchez del Rio M. XOP: A graphical user interface for spectral calculations and X-ray optics utilities. *Review of Scientific Instruments*. 1996;67:3356(4p).
- [53] Bleuet P, Cloetens P, Gergaud P, Mariolle D, Chevalier N, Tucoulou R, Susini J, Chabli A. A hard X-ray nanoprobe for scanning and projection nanotomography. *Review of Scientific Instruments*. 2009;80:056101(3p).
- [54] Beltran M A, Paganin D M, Uesugi K, Kitchen M J. 2D and 3D X-ray phase retrieval of multi-material objects using a single defocus distance. *Optics Express*. 2010;18:6423-6436.